Article

Hybrid Functional Study on Electronic and Optical Properties of the Dopants in Anatase TiO$_2$

W. A. Chapa Pamodani Wanniarachchi,* Thevakaran Arunasalam, Punniamoorthy Ravirajan, Dhayalan Velauthapillai,* and Ponniah Vajeeston

Cite This: ACS Omega 2023, 8, 42275−42289

Read Online

ACCESS | Metrics & More | Article Recommendations

ABSTRACT: TiO$_2$ was known as a golden heterogeneous photocatalyst due to its chemical stability, low cost, nontoxicity, and strong oxidizing power. However, anatase TiO$_2$ predominantly absorbs the photon energy in the ultraviolet region ($\lambda < 387.5$ nm); therefore, to increase the utilization of sunlight, the approach of doping of metals and nonmetals into pure TiO$_2$ is implemented. Here we incorporate the dopants of Zr, Si, V, W, Ge, Cr, Sn, Mo, and Pb into the TiO$_2$ lattice and study the optoelectronic properties, including the formation energies and the electron charge distributions, using the Vienna ab initio Simulation Package (VASP) from the hybrid functional of Heyd, Scuseria, and Erhzerhof (HSE06). We observed that V-, Mo-, and Cr-doped systems introduce shallow impurity states within the band gap, and those states influence the shift of the absorbance spectra to visible light by enhancing the photocatalytic efficiency. W-doped anatase TiO$_2$ structure reduces the band gap of the pure anatase TiO$_2$ by 0.7 eV. Notably, this reduction occurs without the introduction of any impurity states between the band edges. Additionally, the absorption edge of the solar spectrum shifts toward lower photon energy from 3.5 to 3.1 eV. From Bader charge analysis, we observed that mainly the charge transfer occurred from the dopants and charge accumulation happened around nearby oxygen atoms. The ferromagnetism was observed in V-, Cr-, Mo-, and W-doped anatase TiO$_2$ structures due to the charge imbalance of the spin-up and spin-down states.
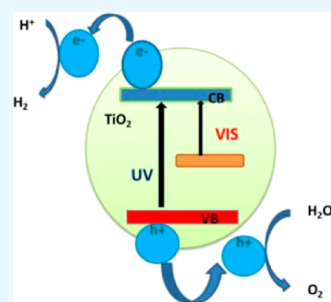
INTRODUCTION

The visible region covers most of the part (43% of the incoming solar energy) in the solar spectrum. The role of photocatalysts is crucial for the utilization of solar energy in this region. Over the previous 20 years, there has been a noteworthy scientific focus on photocatalysts, particularly in processes like water splitting and degradation of the organic contaminants under visible light irradiation.[1] The process of photocatalytic water splitting occurs when the oxide semiconductor absorbs the photon energy. Consequently, if the energy of incoming photons matches the band gap energy of the photocatalytic material, this leads to the separation of the electrons and holes within the photocatalyst. So far, scientists have worked out for these photocatalyst materials, including TiO$_2$, SrTiO$_3$, α-Fe$_2$O$_3$, WO$_3$, ZnO, Bi$_2$WO$_6$, and ZnS.[2] Among them, TiO$_2$ is known as a proficient photocatalyst capable of facilitating self-cleaning surfaces and contributing to the purification of both air and water. Due to its strong oxidation activity and exceptional hydrophilicity, TiO$_2$ was acknowledged as possessing antibacterial properties. Additionally, it retains remarkable chemical stability during the process of photocatalysis. Furthermore, TiO$_2$ is characterized by its nontoxic nature and affordability, thus it has played a significant and engaged role in research areas related to renewable energy. TiO$_2$ exists in three distinct polymorphs:

rutile, anatase, and brookite. These three structural variations arise from different distortions in the octahedral TiO$_6$ configuration. The electronic and optical characteristics are predominantly influenced by the specific characteristics of the Ti−O bonds. The rutile phase is the most stable polymorph, while the remaining two polymorphs are metastable phases. Phase transitions can occur among these three phases depending upon their particle size, high-temperature conditions, pH, and fabrication conditions[3−5]

Mainly rutile and anatase are employed as photocatalysts for water splitting. Anatase TiO$_2$ polymorph offers superior attributes as a photocatalyst compared to rutile. For instance, the surface of anatase TiO$_2$ exhibits greater absorption capacity on hydroxyl groups and a lower recombination rate of photogenerated charge carriers. These attributes are conducive to facilitating the surface chemical reaction.[6] Collectively, these features suggest that the anatase phase of TiO$_2$ holds greater
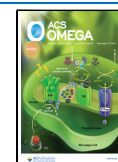
potential as a material for effective photocatalytic activity when compared with the rutile phase.

However, the anatase phase of TiO_2 semiconductor possesses a wide bandgap of around 3.23 eV. The wavelength of light needs to be less than 384 nm to be irradiated on this semiconductor to function as a photocatalyst. However, this particular wavelength range constitutes only about 5% of the solar spectrum, falling within the ultraviolet (UV) region. To utilize most of the solar light that falls to the earth in the visible region, it is essential to adjust the bandgap of TiO_2 accordingly. To overcome this challenge, researchers have developed innovative concepts aimed at tuning the band gap and enhancing photocatalytic performance over the visible region.[2] Researchers have pursued two primary strategies to address this challenge: (1) Bandgap engineering; This approach involves the introduction of specific elements into TiO_2 to enable the absorption of light in the visible region, which can modify the bandgap of the material, allowing it to absorb a broader range of wavelengths, including the visible area of the solar spectra (2) surface sensation; In this strategy, light harvesting materials are applied to sensitize the TiO_2. These materials can absorb visible light and then transfer the absorbed energy to TiO_2 material, thereby enhancing the photocatalytic activity in the visible region.[7]

Theoretically, the majority of calculations involving anatase TiO_2 and its doped structures have been analyzed by using the generalized gradient approximation (GGA) and GGA + U methods.[8,9] In this work, we conducted a comprehensive study aiming at the optoelectronic properties of anatase TiO_2 doped with the elements of Zr, V, W, Cr, Sn, Mo, Si, Ge, and Pb. The majority of the doped structures involving these elements were studied in both theoretical calculations and experimental analyses. Umebayashi et al. reported that the TiO_2-doped V and Cr showed the midgap states where the electrons were occupied and the electrons localized around each dopant.[10] Ibrahim et al. performed density functional theory (DFT) calculations on the monodoped Cr structures, which showed the shallow donor states located above the valence band maximum (VBM) resulted in the band gap narrowing of the undoped TiO_2 lattice, and the partially occupied deep states were found away from the conduction band minimum (CBM). Those impurity states were able to shift the absorption edge to the visible light; however, the deep-level states suppressed the charge separation of electron-hole pairs because they act as the recombination centers for the photoinduced carriers.[11] Soussi et al. observed that the impurity levels within spin-up and spin-down channels were increased as the concentration of Mo in the TiO_2 lattice increased which had a significant impact on effectively reducing the bandgap.[12] It is well known that standard DFT calculations based on LDA and GGA have limitations as they underestimate the band gap values of semiconductors due to the discontinuity of exchange–correlation potential.[13,14] Calculations based on developed exchange correlation functionals included in GGA + U and HSE06 provide accurate band gap values compared with the experimental values. The Cr-doped anatase TiO_2 showed the semimetallic nature under the GGA and GGA + U approximation,[15,16] as experimentally it acts as a ferromagnetic oxide semiconductor.[17] Those approximations have the possibility of providing the wrong predictions. Under the GGA + U approximation, the Hubbard U values are estimated by selecting the U value that aligns with the band gap value of the dopant oxide. For the TiO_2, the U value was 7 eV, which

gives the correct band gap of TiO_2 as 3.2 eV.[18] Likewise, when finding the U values for the dopants, the dopant oxide's band gap value should be approximately derived from the appropriate U values. However, most of the U values of metal oxides do not agree with their band gap values. Therefore, we chose the hybrid functional method to study the optoelectronic properties of the doped anatase TiO_2 models using the density functional theory, which is well-known to reproduce the experimental electronic properties in the periodic crystal lattice. The HSE06 functional was used for the elementally doped TiO_2 by the past theoretical researchers to examine the in-depth calculations of electronic structures, but there is a lack of optical calculations under the hybrid functional method.[19]

In this work, we focus on the electronic and optical calculations of anatase TiO_2-doped models where the dopants are metals (Zr, V, W, Cr, Sn, Mo, and Pb) and nonmetals (Si and Ge), which were analyzed in the HSE06 approximation using VASP software. As discussed above, many attempts have been taken to improve the photocatalytic performance of TiO_2 through the metals (Zr,[20,21] V,[22,23] W,[14] Cr,[15,16] Sn,[24] Mo,[25,26] and Pb[21]) and nonmetals (Si[19,27] and Ge[21]) doping. Due to the high computational cost and time consumption, optical property calculations in the HSE06 approximation were not employed in most of the research works. Here we include both electronic and optical calculations under the HSE06 method, which is a computationally expensive tool but yields accurate results, providing bandgap values that closely align with experimentally derived values for the aforementioned models. This will be worth studying the optoelectronic calculations of the doped anatase TiO_2 with another approach of ab initio investigations rather than the standard DFT methods. Here we described the computational methodologies that were involved in our electronic density of states and the optical properties. Subsequently, we present the obtained results and discuss them along with the previous theoretical and experimental findings. In the end, we conclude our study by summarizing the findings based on the analysis conducted.

■ COMPUTATIONAL METHODOLOGY

The projector-augmented wave (PAW)[28] pseudopotentials were used for all the DFT calculations in the VASP code.[29] Initially, geometry optimization was done for both the pure and doped models in the GGA method, which was parametrized at the Perdew–Burke–Ernzerhof (PBE) level[30] with the Monkhorst–Pack k-point mesh[31] of 4 × 4 × 4. Here we used the plane wave basis set with a cutoff energy of 560 eV for our calculations. For the electronic property calculations, the density of states (DOS) of the doped structures were computed on the Monkhorst–Pack k-point grid on 7 × 7 × 5 along the x, y, and z directions of high symmetry in the first Brillouin zone. All of the doped structures of the DOS calculations were performed using the spin-polarized approach. The electronic and optical property calculations were done in the screened hybrid functional called (Heyd–Scuseria–Ernzerhof) HSE06.[32] This hybrid functional was chosen because it will provide accurate band gap values that closely match the experimental measurements, unlike the results obtained from the GGA method. VESTA is a three-dimensional visualization program that was used to visualize the equilibrium crystal lattices.[33]

The transition metal or nonmetal was doped to the anatase TiO_2 supercell (2 × 2 × 1) and optimized the doped structure

using the GGA approximation. The doped system consists of 48 atoms by 15 titanium atoms, 1 dopant, and 32 oxygen atoms, which corresponds to the 6.25% dopant percentage (Figure 1).
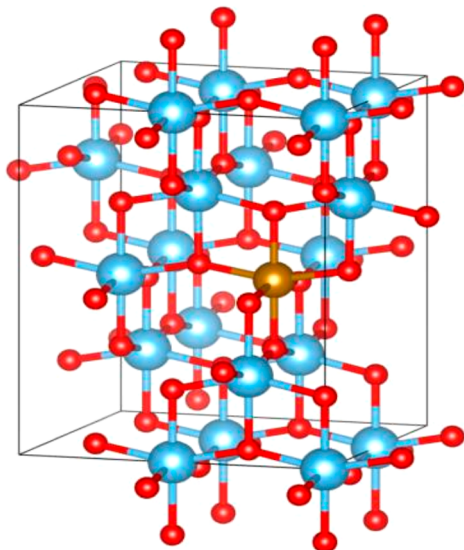

Figure 1. $2 \times 2 \times 1$ supercell of the doped TiO_2 structure. The blue atoms are titanium atoms, the red atoms are denoted as oxygen atoms, and the doped element is represented by the brown color sphere.

RESULTS AND DISCUSSION

Structural Optimization. The total energies and corresponding volumes of the two polymorphic compounds of TiO_2, rutile, and anatase were fitted to the Birch−Murnaghan equation, where the optimization was utilized in GGA. The stability of the anatase phase is higher compared to the rutile phase, as depicted in Figure 2, which consists of the past theoretical results.[34] At elevated temperatures, the rutile phase has the capability of undergoing a transformation into the anatase phase.

Initially, the optimized configurations (at the GGA level) of both the pure and doped systems were achieved. Their equilibrium lattice parameters are tabulated as shown in Table 1. Here the optimization is carried out at the PBE level,

Table 1. Computed Lattice Parameters of the Compounds along with Other Experimental (expt) and Theoretical (Theo) Studies

doped system	lattice parameters (Å)			cell volume (Å^3)
	a	*B*	*c*	
TiO_2-pure (anatase)	3.8179	3.8179	9.7473	142.08
	3.796 (exp.)[35]	3.796 (exp.)[35]	9.444 (exp.)[35]	136.084(exp.)[35]
	3.80 (Theo)[6]	3.8 (Theo)[6]	9.7 (Theo)[6]	140.068 (Theo)[6]
Cr-doped TiO_2	7.6263	7.6263	9.6782	562.88
Mo-doped TiO_2	7.6697	7.6697	9.7020	570.71
Pb-doped TiO_2	7.6762	7.6762	9.8810	582.23
Si-doped TiO_2	7.6016	7.6016	9.6569	558.02
Sn-doped TiO_2	7.6572	7.6572	9.7928	574.18
V-doped TiO_2	7.6332	7.6332	9.6794	563.98
W-doped TiO2	7.6849	7.6849	9.6725	571.24
Zr-doped TiO_2	7.6691	7.6691	9.7760	574.98
Ge-doped TiO_2	7.6261	7.6261	9.7176	565.14

resulting in an overestimation of the cell volume by 1 and 4% in comparison to previous theoretical and experimental studies, respectively,[6,35] with an error of 0.3 Å on the elongation of the lattice parameter in the *c* direction, which was confirmed by Tosoni et al.[36] The anatase TiO_2 with substitutional doping shows minor alterations in its lattice parameters when compared to the undoped anatase TiO_2. All the doped structures maintain the same crystal group as pure TiO_2 called the tetragonal, regardless of the specific dopant element.

Formation Energy. The calculation of the formation energy (described in eq 1) for the doped structures provides
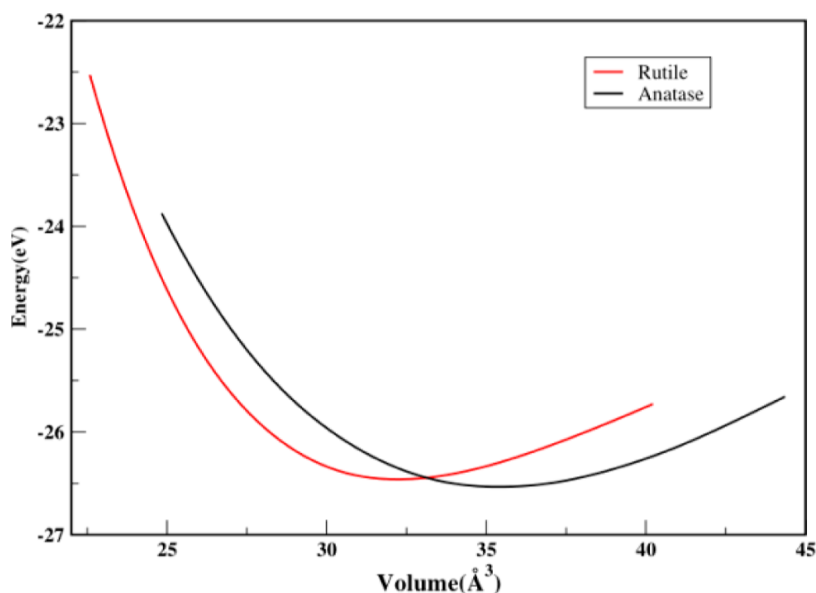

Figure 2. Total energy variation with the volume of both phases of rutile and anatase TiO_2.

insight into their thermal stability, offering valuable guidance for the experimental synthesis procedures.

$$E^f[X^q] = E_{tot}[X^q] - E_{tot}[Ti_{16}O_{32}]$$
$$- \sum_i n_i \mu_i + q[E_F + E_v + \Delta V] \quad (1)$$

Where $E_{tot}[X^q]$ is the total energy of the single impurity-doped TiO_2 supercell structure, and $E_{tot}[Ti_{16}O_{32}]$ is the total energy of the undoped equivalent supercell. n_i is the number of atom types being added or removed, μ_i is the respective chemical potential of the n_i. E_F is the Fermi level reference to the VBM, E_v of the bulk materials. ΔV is simplified as zero.[37,38] In the present work, the formation energy of the single-doped system can be found using eq 2.

$$E^f[X^q] = E_{tot}[X^q] - E_{tot}[Ti_{16}O_{32}] - \mu_{TM} + \mu_{Ti} \quad (2)$$

Here μ_{TM} is the chemical potential of the dopant element. μ_{Ti} is considered to be the total energy of the thermodynamic equilibrium of bulk Ti, while the oxygen chemical potential (μ_O) can be obtained from the thermodynamical condition of the TiO_2, the μ_{Ti}+ 2 $\mu_0 = \mu_{TiO_2}$. The μ_O is the total energy of the molecule of the O_2, the same as the Ti chemical potential that can be obtained from the above stability condition of TiO_2. The formation energies of the dopant elements are listed in Table 2 under the GGA approximation. The computed values for $E_{tot}[Ti_{16}O_{32}]$, μ_O, and μ_{Ti} are equal to −423.89, −4.95, and −11.23 eV, respectively.

Table 2. Formation Energies of the Doped TiO_2 Systems

doped system	μTM/eV	$E_{tot}[X^q]$	$E^f[X^q]$
Cr/TiO$_2$	−9.50	−421.69	0.47
W/TiO$_2$	−13.01	−425.89	−0.22
Mo/TiO$_2$	−10.95	−420.49	3.12
V/TiO$_2$	−8.94	−422.62	−1.03
Si/TiO$_2$	−5.43	−420.02	−1.98
Ge/TiO$_2$	−4.18	−416.37	0.42
Sn/TiO$_2$	−3.83	−415.75	0.74
Pb/TiO$_2$	−3.58	−412.62	3.62
Zr/TiO$_2$	−8.47	−425.55	−4.42

The formation energies ($E^f[X^q]$) for the doped models of 48-atom supercells are derived and listed in Table 2. E^f values are in the order of Zr < Si < V < W < Ge < Cr < Sn < Mo < Pb. The magnitude of the calculated formation energy depends upon the doped structures' electronic structure, charge compensation, atomic size, lattice mismatch, defect formation, chemical compatibility, etc. The specific electronic configuration and charge compensation mechanisms of each dopant play a crucial role in determining the formation energy. Positive formation energies can arise due to the difficulty in accommodating the dopant's electronic structure within the host material's lattice. Some dopants may introduce charge imbalance or create electronic states that are energetically unfavorable, leading to higher formation energies. From the structural point of view; the influence of atomic size and lattice mismatch between the dopant and host material affects the formation energy of these doped models. Dopants with similar atomic sizes to the host lattice elements (e.g., Zr and Si) might be more likely to substitute into the lattice without causing significant distortions, resulting in lower formation energies.

On the other hand, larger or smaller dopants (e.g., W and V) could lead to lattice strain and higher formation energies due to lattice distortion. Another possible mechanism is defect formation. The possibility that certain dopants may form defects or local distortions in the host lattice. These defects can contribute to positive formation energies as they introduce disruptions in the regular lattice arrangement. The type and severity of defects caused by different dopants can vary, impacting the overall formation energy. It should be noted that the chemical compatibility between the dopant and the host material is also very important. Some dopants may have stronger chemical interactions with the host lattice, allowing them to be more readily incorporated with lower formation energies. This compatibility can be influenced by factors such as electronegativity, valence state, and bonding characteristics. The negative formation energies of W, V, Si, and Zr show that they are thermodynamically stable to replace Ti with W, V, Si, and Zr than other dopants. Therefore, W- and V-doped TiO_2 models will be better candidates for optoelectronic applications by considering the optical property calculations where the absorption edge moves toward the visible region. Here, the positive formation energies indicate that the doped anatase models may not be thermodynamically stable under standard conditions, but there is still scientific interest in exploring their properties and behavior. These dopants may be formed as metastable phases, meaning they persist in a nonequilibrium state due to kinetic barriers hindering them from transitioning to the most stable state. External influences like temperature and pressure may alter the thermodynamic landscape. Certain materials can be stabilized at higher temperatures or pressures that are not encountered under standard conditions. Experimentally, most of these elements were used as dopants for the anatase TiO_2.[39,40]

Electronic Properties. The band structure of pristine anatase TiO_2, as illustrated in Figure 3a, exhibits the indirect bandgap feature with the band gap value of 3.4 eV under HSE06 approximation, consistent with previous theoretical investigations.[19] Its partial density of states, depicted in Figure 3b, shows the valence band primarily consists of oxygen 2p orbitals, with little contribution from Ti 3d states and 4p orbitals. The conduction band (CB) is mainly dominated by Ti 3d orbitals. The spin polarization in a pure TiO_2 lattice is not detected, as electrons are evenly distributed in both the spin-up and spin-down states. Similar features of the density of states in undoped TiO_2 structures were explored in prior theoretical works.[21,41,42] The doping with cations in replacement of the Ti^{4+} cation can introduce intermediate energy levels in the pure TiO_2 band structure. These intermediate states act as either electron acceptors or electron donors in pure TiO_2, thereby aiding the material's ability to absorb visible light.

The Zr-doped TiO_2 (Figure 4) exhibits a comparable partial density of states to the undoped TiO_2 structure because both have the same valency four under groups IV-B of transition metals. The band gap is almost similar to that of undoped TiO_2. However, there is a slight extension of 0.09 eV compared to that of pure TiO_2. Notably, there are no impurity levels located within the band gap, aligning with the findings of earlier theoretical investigations.[20,21] The similar partial density of states patterns are evident in the Si-, Ge-, Sn-, and Pb-doped models, all of which possess valency of four in group IV-A identical to the Zr-doped structure (Figures 5−8). The incorporation of Si doping to the pure TiO_2 (Figure 5) leads to a band gap extension of 0.07 eV in comparison to the
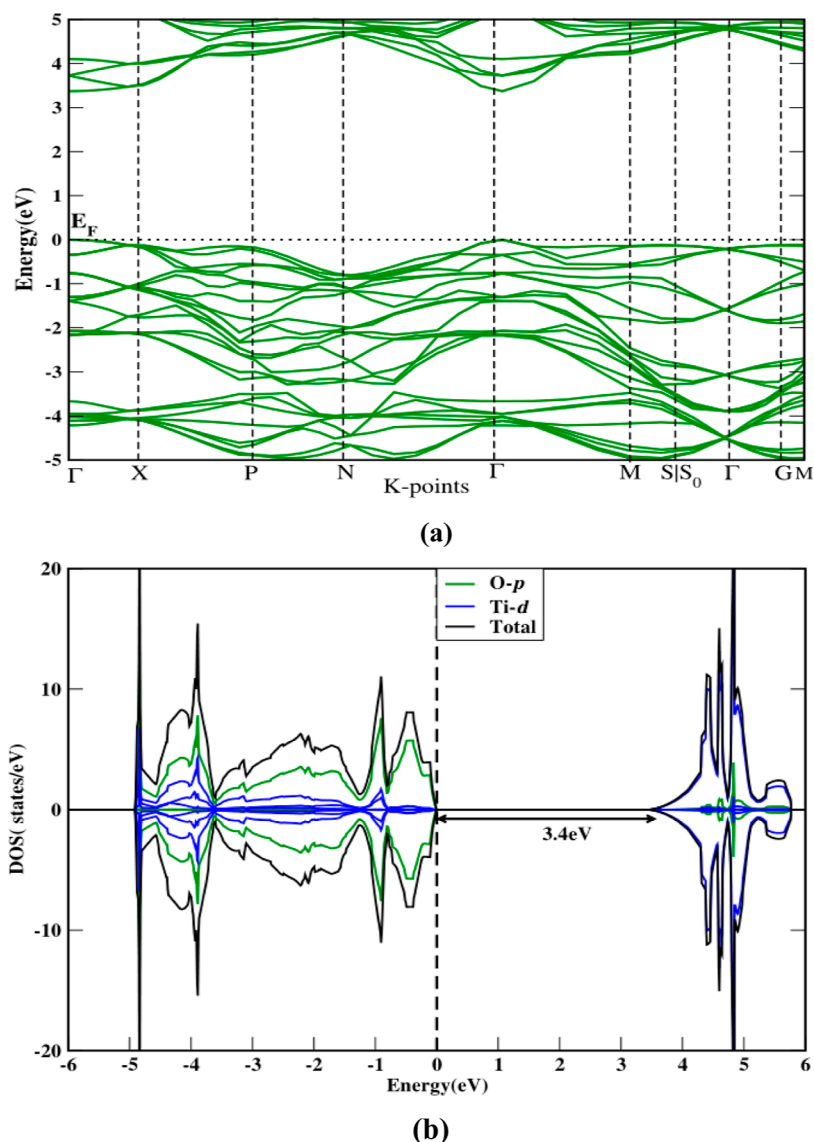
Figure 3. Calculated (a) band structure (top) and (b) partial density of states (bottom) of anatase TiO_2 under the HSE06 approximation.

undoped TiO_2. Theoretical findings demonstrate that the band gap was reduced at a lower concentration of 3%. However, as the concentration was raised to 6, 9, and 12.5%, the band gap of the Si-doped model exhibited an increase which matches with the band gap increment observed in our Si-doped TiO_2 model at a 6% Si concentration.[27] Similar observations were identified in another study conducted using the HSE06 method for these models.[19] The band gap value of the Sn-doped structure increases by approximately 0.1 eV. This finding correlates with the theoretical study indicating where the band gap tends to rise as the Sn content increases in the doping of TiO_2.[24]

The V (Figure 9) and Mo (Figure 10) doped systems have defect states mainly originating from the 3d and 4d orbitals of the V and Mo, respectively. Those states are integrated with the CB, and some are away from the CB and the valence band. Due to the integration of the CB of the V- and Mo-doped TiO_2, the band gap was reduced, facilitating the absorption of visible light. Experimental studies have reported a decrease in the band gap, consequently shifting the absorption spectrum to longer wavelengths.[22,25] Ge- and Pb-doped anatase TiO_2

structures result in an enlargement of the band gap, shifting it from the original value of 3.4 eV (pure TiO_2) to 3.51 and 3.44 eV, respectively. The extension is approximately 0.11 eV for Ge- and 0.04 eV for Pb-doped models. In the case of the V-doped system (as shown in Figure 9), the energy difference between the VBM and defect states is 1.1 eV, which is less than the energy gap of 2.2 eV separating the defect states and the CBM. Additionally, the band gap of the V-doped model is reduced by 0.1 eV compared with pure anatase TiO_2. These intermediate states are located near the VBM, and they act as shallow acceptor levels, primarily comprising the V 3d orbitals. Those states have the potential to trap the photoexcited holes, thereby mitigating the recombination rate of electron−hole pairs. Due to the creation of electron vacancies near the valence band, an anodic photocurrent can be produced. Here more probability can be predicted for the excitation of electrons to the intermediate states where the low photon energy is sufficient to jump the electrons into the CB. As a result of this occurrence, we could expect the visible light absorption for the V-doped model system. The reduction in
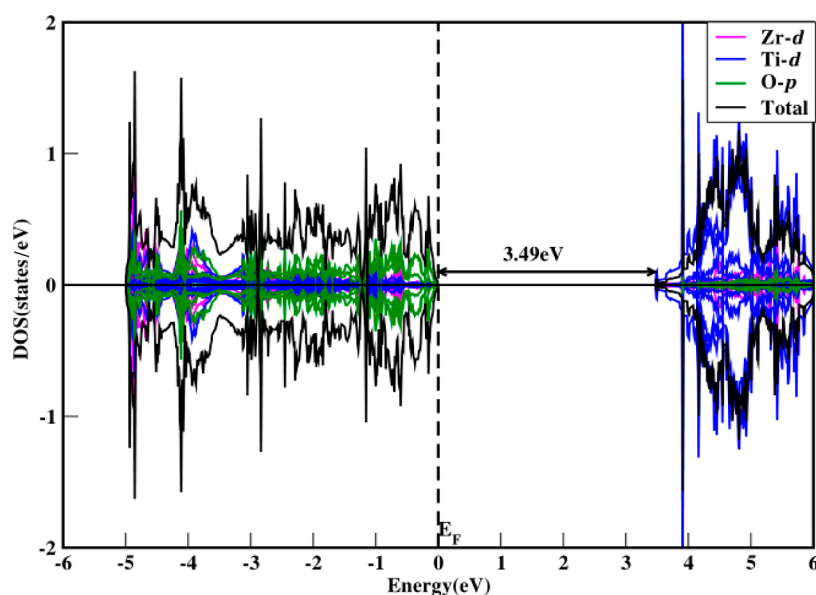
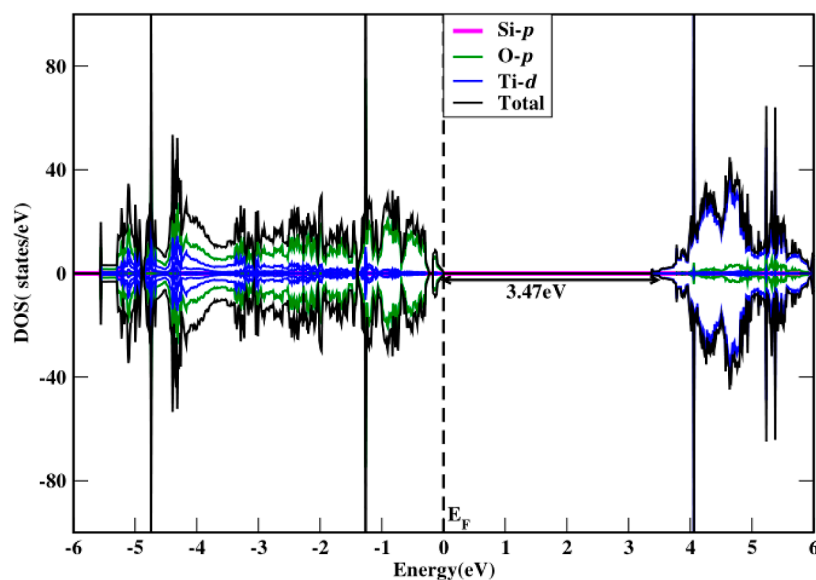**Figure 4.** Density of states of Zr-doped anatase TiO$_2$ using the HSE06 functional.

Figure 5. Density of states of Si-doped anatase TiO$_2$ using the HSE06 functional.

the band gap of the V-doped system has been documented in previous experimental investigations.[22,43]

In the Mo-doped system (Figure 10), there is a noticeable shift of the Fermi level toward the CB. This would be a potential benefit for the photocatalytic performances as free electrons are moving in the CB. These findings align with the previous observations seen in monodoped Mo in anatase TiO$_2$ under the GGA and GGA + U approximations.[25,26] The electrons are more likely to be excited from the defect states to the CB than the electrons' transitions from the valence band to the defect states. This occurrence is due to the energy gap between the valence band and defect states being 2.38 eV, which is greater than the energy gap of 0.98 eV between the defect states and the CB. Those defect states composed of the hybridization of Mo-4d–Ti-3d states are located at a certain distance away from the CB and act as shallow donor states. This phenomenon also contributes to lowering the recombination rate of the charge carriers in semiconductors by

trapping the photogenerated electrons, and it will produce the cathodic photocurrent. The reduction of the band gap can be seen in the W-doped TiO$_2$ by about 0.7 eV, as shown in Figure 12. Here the Fermi level resides in the CB, similar to the Mo-doped configuration. This alignment adheres to both the Mossec-Burstein effect and the Urbach band-tail effect, leading to the population of the CB by the electrons.[44] Nevertheless, there are no impurity states found within the band gap of the W-doped model; this absence of impurity states prevents the electron−hole recombination, which has the potential to enhance the photocatalytic efficiency.

The Cr-doped structure (Figure 11) consists of shallow donor states that play a beneficial role in facilitating the separation of the electron−hole pairs, much like those in the V- and Mo-doped systems. The presence of defect states of the 3d orbitals of chromium has been identified in other theoretical findings that investigate the substitutional doping of chromium atoms into the anatase TiO$_2$ using the GGA + U
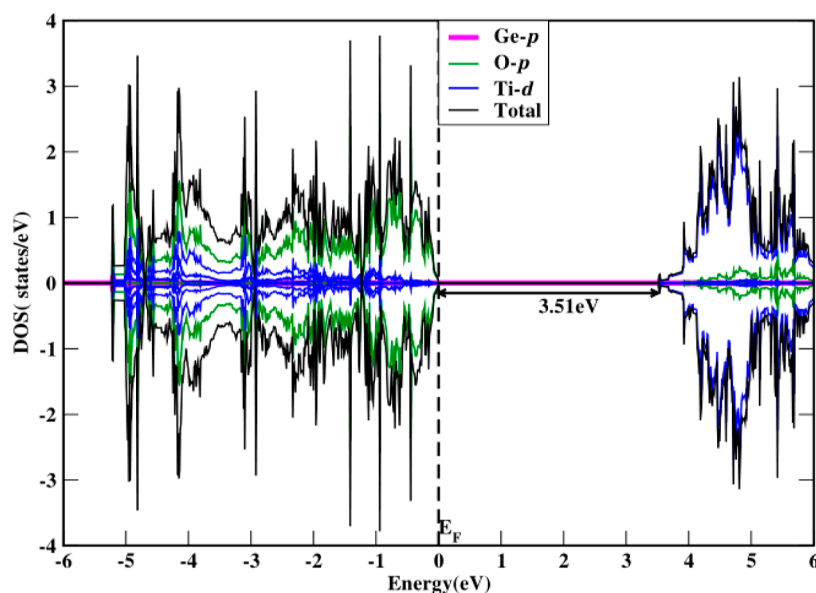
Figure 6. Density of states of Ge-doped anatase TiO$_2$ using the HSE06 functional.
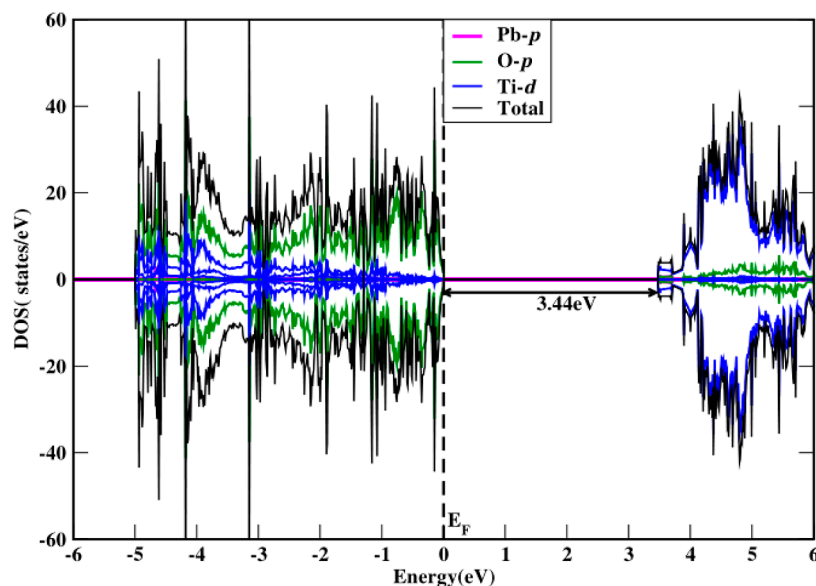

Figure 7. Density of states of Pb-doped anatase TiO$_2$ using the HSE06 functional.

approximation.[16] Nonetheless, prior theoretical works which were carried out on Cr-doped anatase TiO$_2$ under the GGA approximation revealed the half-metallic characteristic of the doped structure where the Cr states are positioned across the Fermi level.[15] However, experimental evidence[17] proved that the Cr-doped model displays semiconductor behavior that can support our HSE06 calculations. Furthermore, the Cr-doped model structure exhibits a wider CB and valence band. This broadening effect contributes to an increased mobility of the electron−hole pairs, which will positively impact the photoactivity of TiO$_2$. All three doped models of V, Cr, and Mo feature shallow impurity states rather than deep defect states. Consequently, this characteristic will be a pivotal factor for elevating photocatalytic efficiency due to promoting the charge carrier separation rather than acting as recombination centers. (The Fermi level is represented as E$_F$ in all the density of states diagrams).

Optical Properties. In this section, the optical property calculations were described using the complex dielectric function, $\varepsilon(\omega)$, as shown in eq 3.

$$\varepsilon(\omega) = \varepsilon_1(\omega) + \varepsilon_2(\omega) \tag{3}$$

The imaginary part of the dielectric function is shown by[45]

$$\varepsilon_2(\omega) = \left(\frac{4\pi^2 e^2}{m^2\omega^2}\right)\sum_{i,j} \times \int_k \langle i|M|j\rangle^2 f_i(1 - f_j)\delta$$
$$(E_{j,k} - E_{i,k} - \omega)\mathrm{d}^3 k \tag{4}$$

where M is the momentum matrix, k is the crystal wave vector, and i and j are the initial and final states along with their energies of $E_{i,k}$ and $E_{j,k}$, respectively.

The real part of $\varepsilon(\omega)$ was derived (eq 5) using the $\varepsilon_2(\omega)$ from the Kramers−Kronig relationship
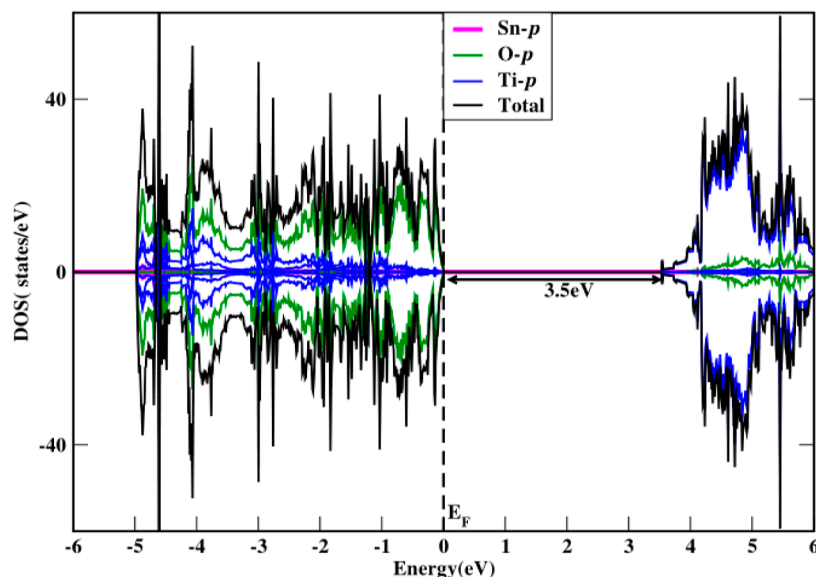
Figure 8. Density of states of Sn-doped anatase TiO$_2$ using the HSE06 functional.
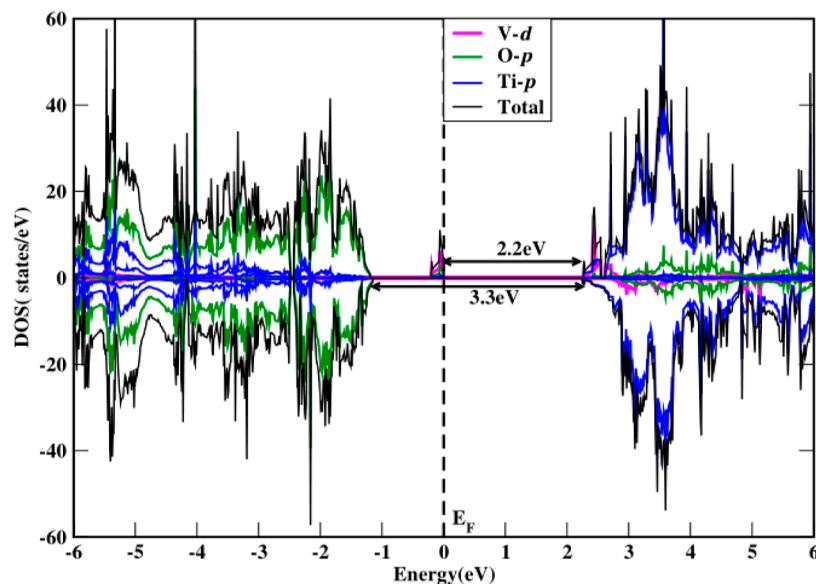

Figure 9. Density of states of V-doped anatase TiO$_2$ using the HSE06 functional.

$$\varepsilon_1(\omega) = 1 + \frac{2}{\pi} P \int_0^\infty \frac{\omega' \varepsilon_2(\omega') \mathrm{d}\omega'}{\omega'^2 - \omega^2} \quad (5)$$

Using $\varepsilon_1(\omega)$ and $\varepsilon_2(\omega)$, other linear frequency-dependent properties can be derived, where the absorption coefficient, $\alpha(\omega)$ is one of the derivations that can be illustrated as[46]

$$\alpha(\omega) = \frac{\sqrt{2}\,\omega}{c} \{[\epsilon_1^2(\omega) + \epsilon_2^2(\omega)]^{1/2} - \epsilon_1(\omega)\}^{1/2} \quad (6)$$

Here we mainly concentrate on the absorption coefficient for all of the doped systems. The optical absorption spectra were computed for the doped models utilizing the HSE06 approximation. Pure TiO$_2$ can absorb the photon energy within the ultraviolet (UV) region. This is illustrated in the optical spectrum diagrams. The presence of intermediate states between the valence band and CB in metal-doped systems, along with the reduction in the band gap of TiO$_2$, causes the absorption edge of optical spectra to move toward the visible

light range (Figures 13 and 14b). This occurs as a result of the electron transition from the O-2p states to the Ti-3d states through the doped elements' valency states. Based on the electronic property calculations, the impurity states are located within the band gaps of V-, Cr-, and Mo-doped anatase TiO$_2$ structures. As a consequence, this led to a shift in the absorbance spectra toward the visible light region with a higher absorbance of 10^5 cm^{-1}, as depicted in Figure 13. V-, Cr-, and Mo-doped anatase TiO$_2$ models shift the absorption edge of pure TiO$_2$ from 3.5 to 2.37, 1.67, and 2.29 eV, respectively. A similar optical absorbance was observed for the Cr monodoped situation, where the absorption edge extended into the visible light region.[11,42] The previous study shows that the absorption edge of Mo-doped anatase TiO$_2$ at the energy of 1.2 eV absorbs the visible light region.[26] They discussed that those electrons' excitations occurred due to the electron transitions from the O-2p to Mo-4d states. Another study noted that an additional absorption occurred below the absorption edge of
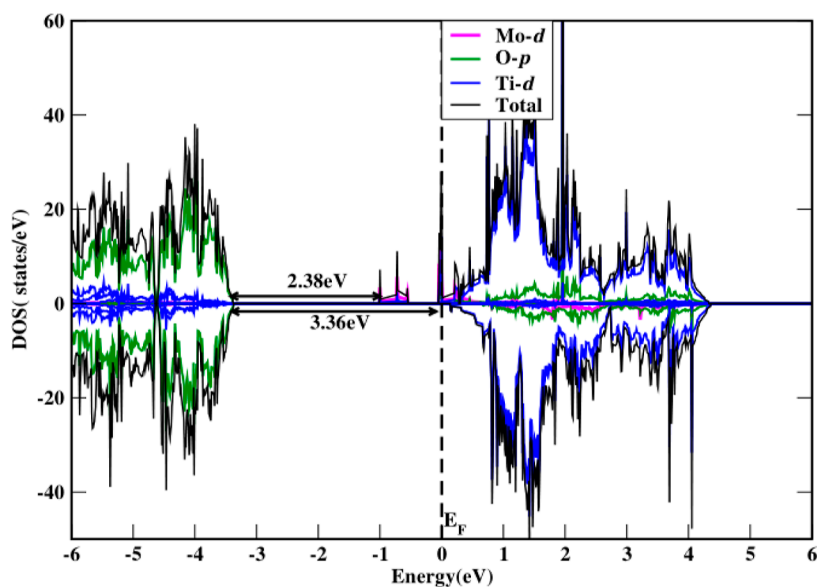
Figure 10. Density of states of Mo-doped anatase TiO_2 using the HSE06 functional.
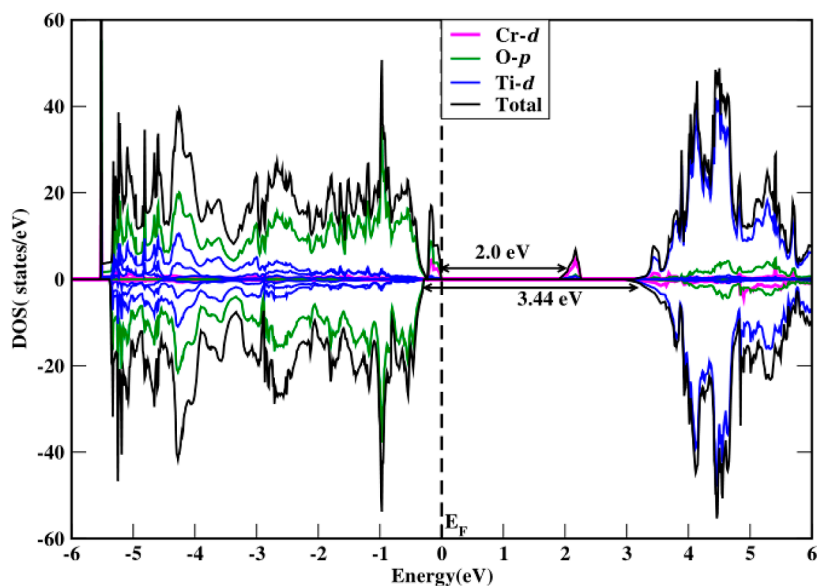

Figure 11. Density of states of Cr-doped anatase TiO_2 using the HSE06 functional.

the Mo-doped system where the electrons' intraband transitions influenced between the Mo-4d impurity band and Ti-3d states in the CB.[47] Our V-doped optical absorption (Figure 13b) yielded an outcome similar to the experimental findings because it absorbs visible light in the range of 2.7−2.5 eV.[48] The theoretical study explains that the visible light absorption of the V-doped model was due to the presence of V^{4+} ions in the crystal lattice that enabled the electron transitions from V-3d states to the host CBM.[23] Another experiment involving the heavy doping of vanadium on TiO_2 revealed a notable redshift, particularly evident with higher vanadium doping concentrations, within the visible range of 380−750 nm.[22] These experimental findings agree with our HSE06 results. Hence, anatase TiO_2 models doped with V, Cr, and Mo efficiently harness solar power, where the absorbance is red-shifted, thereby enhancing the absorption of visible light.

The Si-doped anatase TiO_2 model shows the absorbance that is blue-shifted (Figure 14a), aligning with the experimental

results observed in Si-doped TiO_2 nanotube arrays where the enhancement of photo response occurred under the UV region.[49] A different experimental study provided evidence that the Si-doped TiO_2 nanotubes improved the methylene blue photocatalytic degradation activity of the TiO_2 nanotubes, and the highest degradation efficiency was observed at 10% dopant concentration under ultraviolet light conditions.[50]

Sn-doped TiO_2 showed the blue-shifted absorption curve (Figure 15a), in line with both theoretical and experimental findings. In theoretical calculations using the DFT approach with the GGA approximation, it was calculated that the band gap of Sn-doped anatase TiO_2 broadened by about 0.06 eV, while experimental findings indicated a broader band gap increase of about 0.13 eV. These findings collectively suggest that Sn-doped TiO_2 induces the blueshift of the absorption spectra in pure anatase TiO_2.[21,24] Zr- and Ge-doped anatase TiO_2 structure models exhibit a blueshift of the absorption spectra (Figure 16) due to the extension of the band gap of
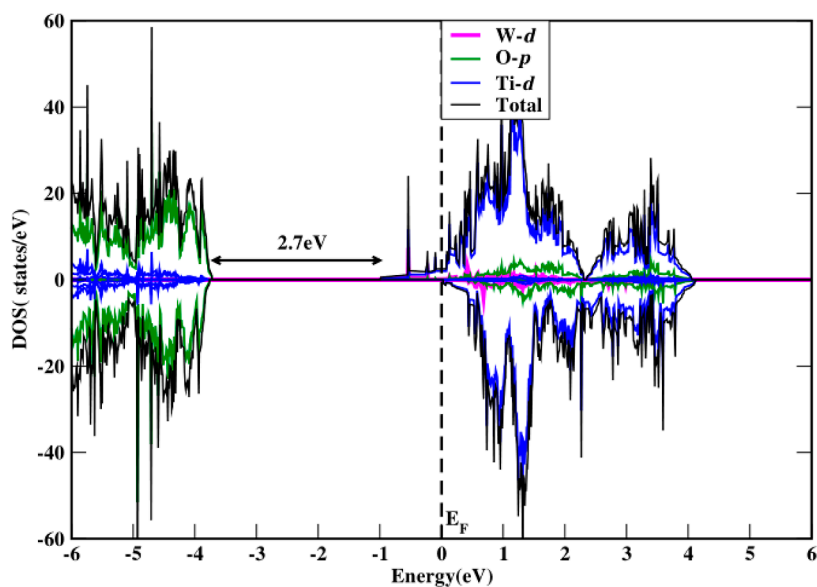
Figure 12. Density of states of W-doped anatase TiO_2 using the HSE06 functional.
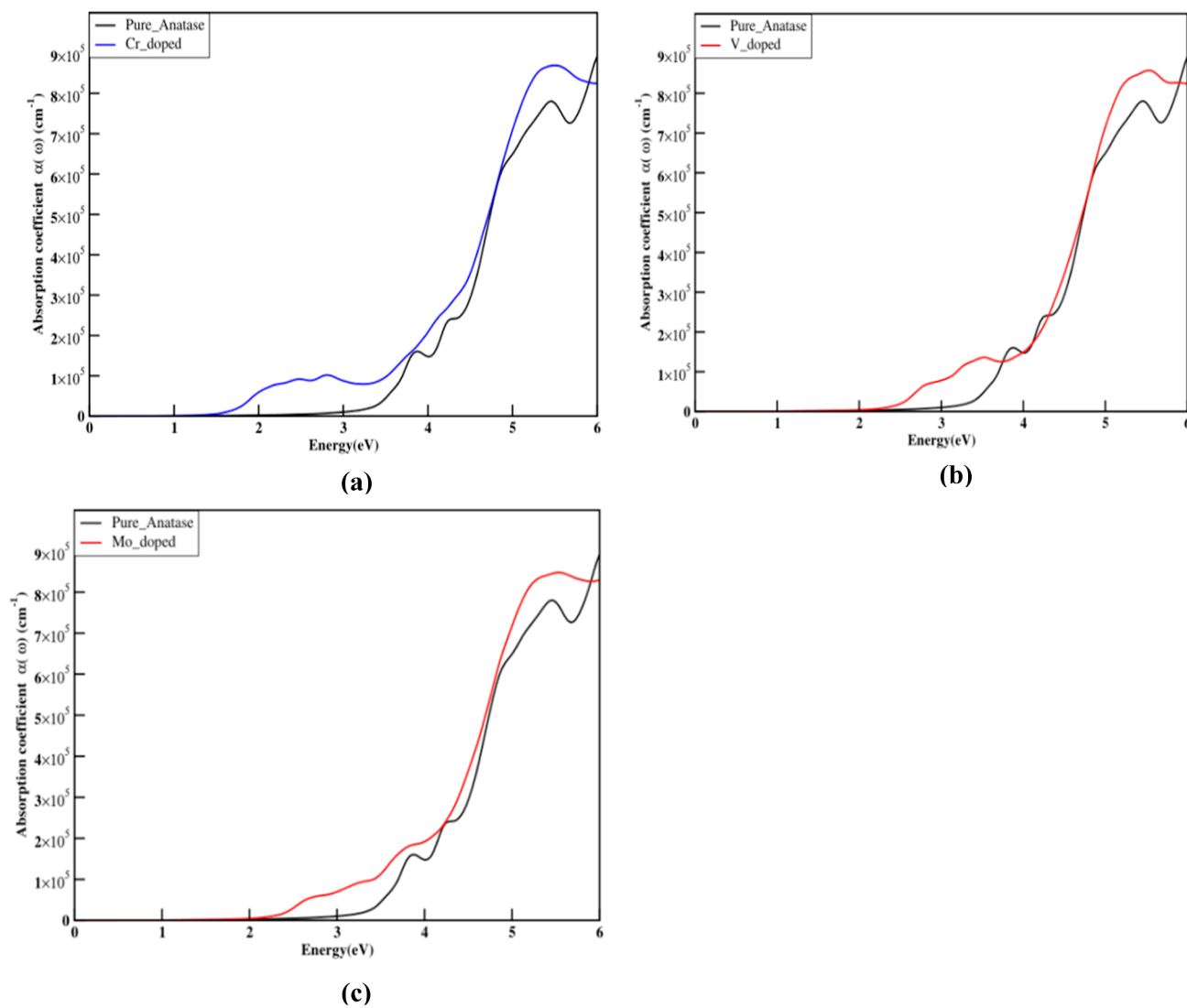

(a)

(b)

(c)

Figure 13. Computed absorption coefficient for the (a) Cr-, (b) V-, and (c) Mo-doped anatase TiO_2 in the HSE06 approximation.
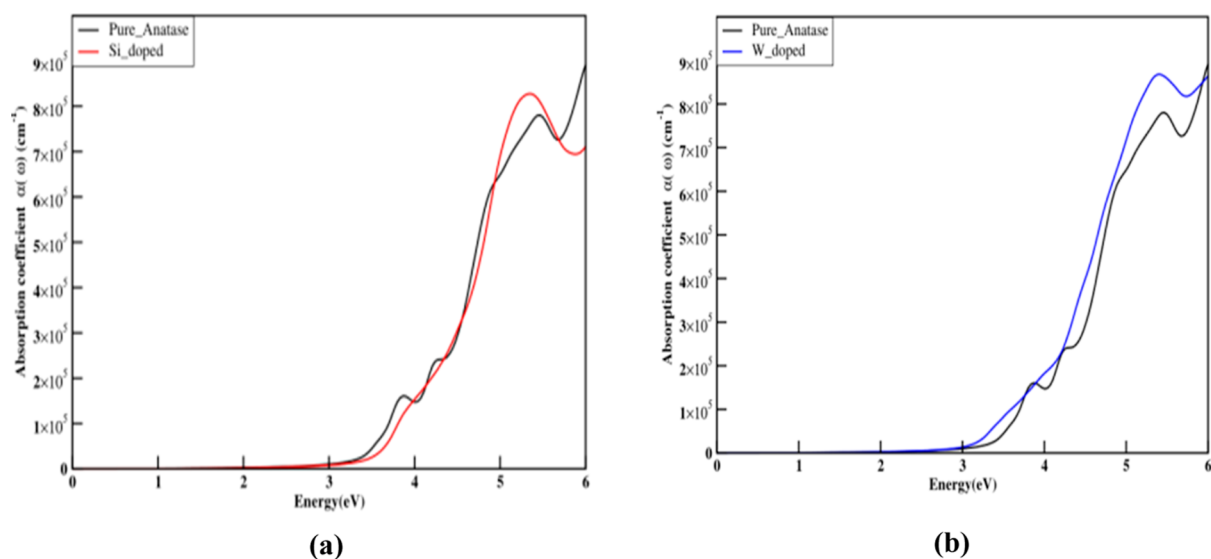
Figure 14. Computed absorption coefficient for the (a) Si- (b) W-doped anatase TiO$_2$ in the HSE06 approximation.
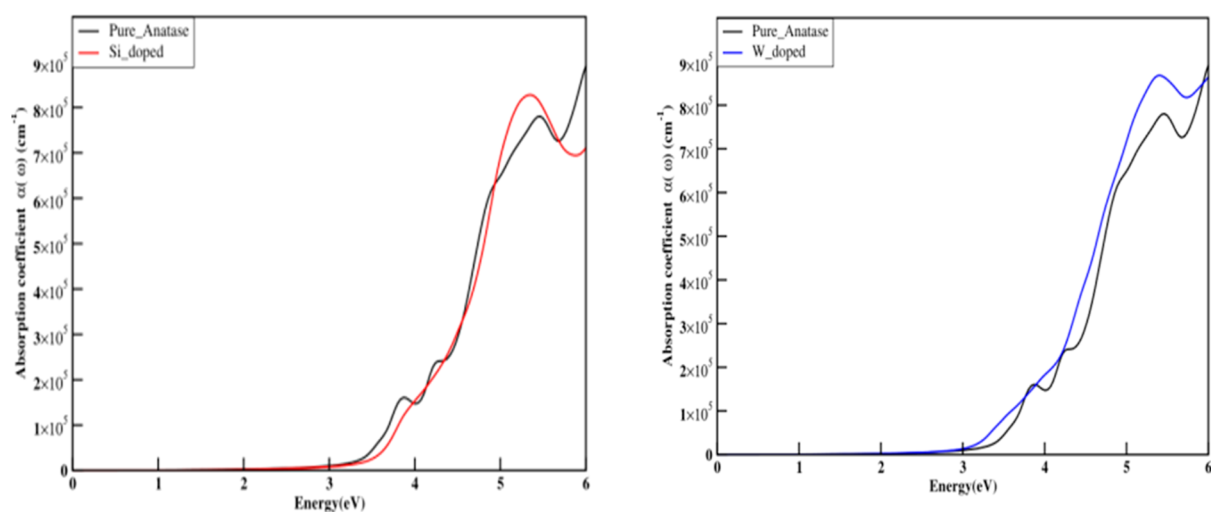

Figure 15. Computed absorption coefficient for the (a) Sn- (b) Pb-doped anatase TiO$_2$ in the HSE06 approximation.
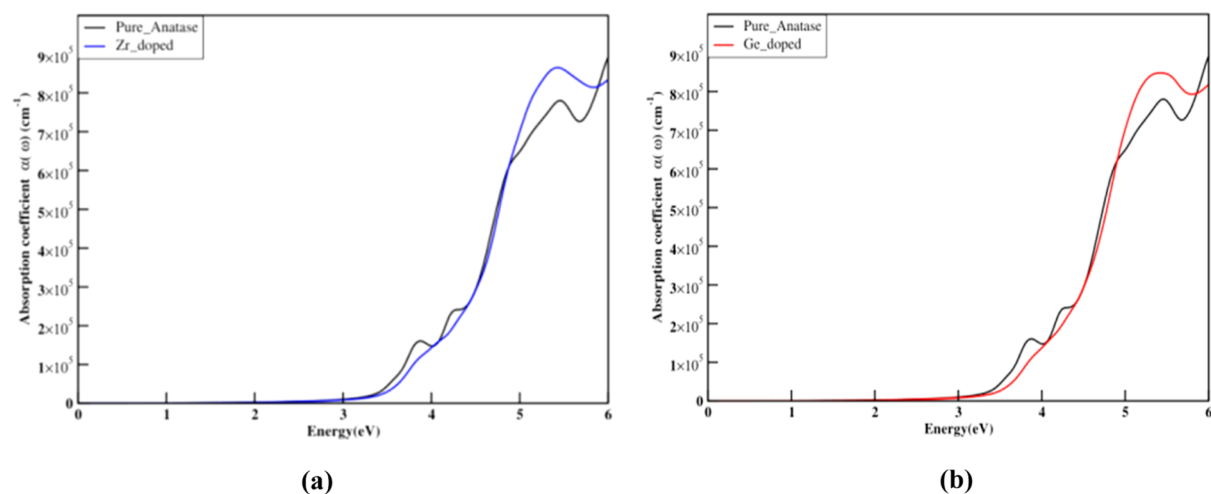

Figure 16. Computed absorption coefficient for the (a) Zr- (b) Ge-doped anatase TiO$_2$ in the HSE06 approximation.

undoped TiO$_2$. In a previous theoretical study conducted using the GGA approximation, it was noted that the blue shift in Zr-

doped anatase TiO$_2$ occurred due to the extension of the band gap when the impurity percentage reached 4.17%.[38] The Pb-
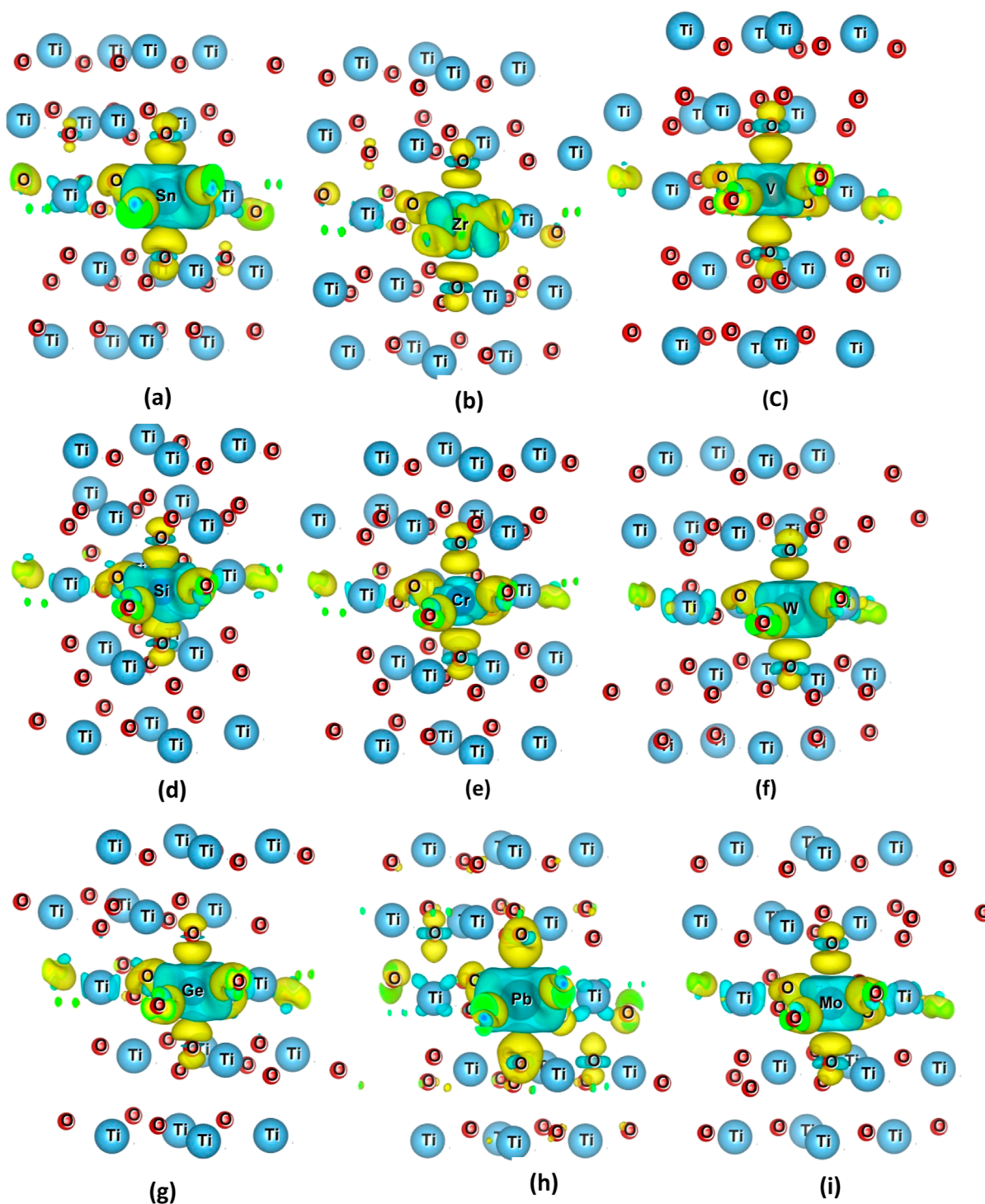
Figure 17. Charge density difference of elemental doped anatase TiO$_2$. (a) Sn-, (b) Zr-, (c) V-, (d) Si-, (e) Cr-, (f) W-, (g) Ge-, (h) Pb-, and (i) Mo-doped systems. Yellow and cyan colors represent the charge accumulation and depletion, respectively.

doped anatase TiO$_2$ model displays the blueshift of the absorption spectra (Figure 15b), which agrees with the theoretical investigation of the Pb-doped anatase TiO$_2$. This consistency is attributed to the extension of the band gap value by 0.02 eV.[21] W-doped TiO$_2$ model shows the redshift of the absorbance spectra, transitioning from 3.5 to 3.1 eV as shown in Figure 14b. Our HSE06 calculations are well correlated with the past experimental findings, wherein the W-doped TiO$_2$ model demonstrated a red shift as the concentration of W dopant in the regular TiO$_2$ lattice increased.[51,52]

Bader Charge Distribution. The Bader charge (BC) analysis was conducted for all of the doped structures, and the resulting charge distribution plots are presented in Figure 17. The charge imbalance can occur when a foreign atom is introduced into the regular TiO$_2$ lattice. The charge density difference, $\Delta\rho_{\text{Chargedifference}}$, which was computed in the self-consistency scheme by subtracting the electron density of the doped system, $\rho_{\text{DopedSystem}}$ from the electron density of undoped, ρ_{pure} and the dopant, ρ_{Dopant}, respectively. i.e.,

$$\Delta\rho_{\text{Chargedifference}} = \rho_{\text{DopedSystem}} - \rho_{\text{pure}} - \rho_{\text{Dopant}}.$$

The Bader charges were used to quantify the charge transfer of the dopant to the lattice, and this information is presented in Table 3. Each of the dopants exhibits electron loss, as

Table 3. Bader Charge [in Units of Electron Charge (e^-)] Analysis on Ti, O, and the Dopant (M), Where M = Mo, V, Cr, Si, Sn, Ge, Pb, W, Zr, and the Magnetic Moment for all the Doped Models

doped system	Bader charges			magnetic moment (μB)
	Ti	O	M	
pure TiO_2	1.94	−0.97		0
Mo@TiO_2	1.90	−0.97	2.2	1.923
V@TiO_2	1.93	−0.97	1.93	0.96
Cr@TiO_2	1.92	−0.96	1.8	1.98
Si@TiO_2	1.93	−0.98	3.09	0
Sn@TiO_2	1.94	−1.0	2.31	0
Ge@TiO_2	1.93	−1.0	2.2	0
Pb@TiO_2	1.93	−1.0	1.86	0
W@TiO_2	1.92	−0.97	2.55	0.763
Zr@TiO_2	1.95	−0.97	2.23	0

indicated by their positive Bader charge values, implying their role as electron donors. In the Mo-doped model, it is observed that the Mo atom carries a charge of $2.2e$. Additionally, nearby oxygen atoms display a charge accumulation of $-0.97e$, while the adjacent Titanium (Ti) atoms exhibit a charge depletion of $+1.9e$. Likewise, the dopant and the neighboring titanium atoms release the electrons, while the adjacent oxygen atoms tend to attract electrons, as shown in Figure 17. This alignment with the BC analysis is shown in Table 3. More electron charge depletion occurs around the dopant compared to the Ti atom. This discrepancy can be attributed to the higher and analogous oxidation states (Mo^{6+}, V^{5+}, Cr^{6+}, W^{6+}, Si^{4+}, Pb^{4+}, Sn^{4+}, Ge^{4+}, and Zr^{4+}) of the dopants in contrast to the Ti (Ti^{4+}) atoms. Due to the higher electronegativity of oxygen atoms compared to both the dopants and Ti atoms, they exert a stronger attraction on electrons, drawing more electrons toward them. Mo-, Cr-, W-, and V-doped systems exhibit magnetic moments arising from the asymmetric nature of spin-up and spin-down channels, which is clearly depicted in the above electronic density of states diagrams (Figures 9, 10, 11, and 12). They are stable in the ferromagnetic state as they exhibit positive magnetic moments.[53] The other doped models remain in the paramagnetic property since their total net spin values sum up to zero. The ferromagnetism has been observed in the structures of TiO_2 doped with V and Cr, confirmed through both theoretical and experimental investigations.[17,53,54] Experimental evidence supports the assertion that Mo-doped anatase TiO_2 displays ferromagnetism at room temperature, attributed to the overlapping of Mo-4d and O-2p orbitals.[55]

CONCLUSIONS

In summary, we performed the electronic, optical, and formation energy calculations for Zr-, Si-, V-, W-, Ge-, Cr-, Sn-, Mo-, and Pb-doped anatase TiO_2. The doping is energetically favorable in the order of Zr < Si < V < W < Ge < Cr < Sn < Mo < Pb. Here W, V, Si, and Zr have shown negative formation energies making them thermodynamically stable when substituting these foreign atoms to the regular TiO_2 lattice. The intermediate states and the bandgap reduction of the host compound were not found for the Zr-, Si-, Ge-, Pb-, and Sn-doped structures. Also, the optical spectra

were shifted to higher photon energies. Therefore, these dopants will not affect the efficiency of the optoelectronic applications rather than the undoped anatase TiO_2. V-, Mo-, and Cr-doped models include the impurity levels within the band gap as shallow and deep defect states; the Mo-doped structure consists of the shallow defect states where the Fermi level is located in the CB. These three dopants and the W-doped model where there are no impurity states located but the band gap reduction occurred with the redshift of the optical spectra. Also, those models show the nature of ferromagnetism, which can be considered as magnetic semiconductors, and the charge density difference analysis shows that charge depletion occurs around the dopant. These V-, Mo-, Cr-, and W-doped models will enhance the photocatalytic efficiency more than the pure anatase TiO_2.

■ AUTHOR INFORMATION

Corresponding Authors

W. A. Chapa Pamodani Wanniarachchi − *Clean Energy Research Laboratory (CERL), Department of Physics, University of Jaffna, Jaffna 40000, Sri Lanka; Faculty of Engineering, Western Norway University of Applied Sciences, Bergen 5020, Norway*; Email: chapa@univ.jfn.ac.lk

Dhayalan Velauthapillai − *Faculty of Engineering, Western Norway University of Applied Sciences, Bergen 5020, Norway*; ⊙ orcid.org/0000-0002-4162-7446; Email: Dhayalan.Velauthapillai@hvl.no

Authors

Thevakaran Arunasalam − *Clean Energy Research Laboratory (CERL), Department of Physics, University of Jaffna, Jaffna 40000, Sri Lanka*

Punniamoorthy Ravirajan − *Clean Energy Research Laboratory (CERL), Department of Physics, University of Jaffna, Jaffna 40000, Sri Lanka*

Ponniah Vajeeston − *Department of Chemistry, Center for Materials Science and Nanotechnology, University of Oslo, Blindern N-0315 Oslo, Norway*

Complete contact information is available at:
https://pubs.acs.org/10.1021/acsomega.3c04329

Notes

The authors declare no competing financial interest.

■ REFERENCES

(1) Tang, J.; Zou, Z.; Ye, J. Photocatalytic Decomposition of Organic Contaminants by Bi 2WO6 under Visible Light Irradiation. *Catal. Lett.* **2004**, *92* (1/2), 53−56.

(2) Zhao, Z.; Liu, Q. Designed Highly Effective Photocatalyst of Anatase TiO2 Codoped with Nitrogen and Vanadium under Visible-Light Irradiation Using First-Principles. *Catal. Lett.* **2008**, *124* (1−2), 111−117.

(3) Hu, Y.; Tsai, H. L.; Huang, C. L. Effect of Brookite Phase on the Anatase-Rutile Transition in Titania Nanoparticles. *J. Eur. Ceram. Soc.* **2003**, *23* (5), 691−696.

(4) Kandiel, T. A.; Robben, L.; Alkaima, A.; Bahnemann, D. Brookite versus Anatase TiO2 Photocatalysts: Phase Transformations and Photocatalytic Activities. *Photochem. Photobiol. Sci.* **2013**, *12* (4), 602−609.

(5) Wu, S.; Luo, X.; Long, Y.; Xu, B. Exploring the Phase Transformation Mechanism of Titanium Dioxide by High Temperature in Situ Method. *IOP Conf. Ser. Mater. Sci. Eng.* **2019**, *493* (1), 012010.

(6) Zhang, J.; Zhou, P.; Liu, J.; Yu, J. New Understanding of the Difference of Photocatalytic Activity among Anatase, Rutile and Brookite TiO2. *Phys. Chem. Chem. Phys.* **2014**, *16* (38), 20382−20386.

(7) Diebold, U. The Surface Science of Titanium Dioxide. *Surf. Sci. Rep.* **2003**, *48* (5−8), 53−229.

(8) Khan, M.; Xu, J.; Chen, N.; Cao, W. Electronic and Optical Properties of Pure and Mo Doped Anatase TiO2 Using GGA and GGA+U Calculations. *Phys. B Condens. Matter* **2012**, *407* (17), 3610−3616.

(9) Zhang, R.; Zhao, J.; Yang, Y.; Lu, Z.; Shi, W. Understanding Electronic and Optical Properties of La and Mn Co-Doped Anatase TiO2. *Comput. Condens. Matter* **2016**, *6*, 5−17.

(10) Umebayashi, T.; Yamaki, T.; Itoh, H.; Asai, K. Analysis of Electronic Structures of 3d Transition Metal-Doped TiO2 Based on Band Calculations. *J. Phys. Chem. Solids* **2002**, *63* (10), 1909−1920.

(11) Ibrahim, H. H.; Mohamed, A. A.; Ibrahim, I. A. M. Electronic and Optical Properties of Mono and Co-Doped Anatase TiO2: First Principles Calculations. *Mater. Chem. Phys.* **2020**, *252*, 123285.

(12) Soussi, A.; Ait hssi, A.; Boulkaddat, L.; Boujnah, M.; Abouabassi, K.; Haounati, R.; Asbayou, A.; Elfanaoui, A.; Markazi, R.; Ihlal, A.; Bouabid, K.; El Biaze, N. First Principle Study of Electronic, Optical and Electrical Properties of Mo Doped TiO2. *Comput. Condens. Matter* **2021**, *29*, No. e00606.

(13) Jung, J. Y.; Park, J. H.; Jeong, Y. J.; Yang, K. H.; Choi, N. K.; Kim, S. H.; Kim, W. J. Involvement of Bcl-2 Family and Caspases Cascade in Sodium Fluoride-Induced Apoptosis of Human Gingival Fibroblasts. *Korean J. Physiol. Pharmacol.* **2006**, *10* (5), 289−295.

(14) Li, M.; Zhang, J.; Zhang, Y. First-Principles Calculation of Compensated (2N, W) Codoping Impacts on Band Gap Engineering in Anatase TiO2. *Chem. Phys. Lett.* **2012**, *527*, 63−66.

(15) Gao, G. Y.; Yao, K. L.; Liu, Z. L.; Li, Y. L.; Jiang, J. L.; Li, Y. C. Half-Metallic Ferromagnetism of Cr-Doped Rutile TiO2: A First-Principles Pseudopotential Study. *Phys. B Condens. Matter* **2006**, *382* (1−2), 14−16.

(16) Yang, K.; Dai, Y.; Huang, B. Density Functional Characterization of the Electronic Structure and Visible-Light Absorption of Cr-Doped Anatase TiO2. *ChemPhysChem* **2009**, *10* (13), 2327−2333.

(17) Kaspar, T. C.; Droubay, T.; Shutthanandan, V.; Heald, S. M.; Wang, C. M.; McCready, D. E.; Thevuthasan, S.; Bryan, J. D.; Gamelin, D. R.; Kellock, A. J.; Toney, M. F.; Hong, X.; Ahn, C. H.; Chambers, S. A. Ferromagnetism and Structure of Epitaxial Cr-Doped Anatase TiO2 Thin Films. *Phys. Rev. B: Condens. Matter Mater. Phys.* **2006**, *73* (15), 155327.

(18) Li, C.; Zhao, Y. F.; Gong, Y. Y.; Wang, T.; Sun, C. Q. Band Gap Engineering of Early Transition-Metal- Doped Anatase TiO 2 : First Principles Calculations. *Phys. Chem. Chem. Phys.* **2014**, *16*, 21446−21451.

(19) Liu, J.; Weng, M.; Li, S.; Chen, X.; Cen, J.; Jie, J.; Xiao, W.; Zheng, J.; Pan, F. High-Throughput HSE Study on the Doping Effect in Anatase TiO2. *Phys. Chem. Chem. Phys.* **2020**, *22* (1), 39−53.

(20) Li, B.; Tang, N. Study on Zr, Sn, Pb, Si and Pt Doped TiO2 Photoanode for Dye-Sensitized Solar Cells: The First-Principles Calculations. *Chem. Phys. Lett.* **2022**, *799*, 139636.

(21) Long, R.; Dai, Y.; Meng, G.; Huang, B. Energetic and Electronic Properties of X- (Si, Ge, Sn, Pb) Doped TiO 2 from First-Principles. *Phys. Chem. Chem. Phys.* **2009**, *11* (37), 8165−8172.

(22) Wu, J. C. S.; Chen, C. H. A Visible-Light Response Vanadium-Doped Titania Nanocatalyst by Sol-Gel Method. *J. Photochem. Photobiol., A* **2004**, *163* (3), 509−515.

(23) Long, R.; English, N. J. First-Principles Calculation of Electronic Structure of V-Doped Anatase TiO2. *ChemPhysChem* **2010**, *11* (12), 2606−2611.

(24) Long, R.; Dai, Y.; Huang, B. Geometric and Electronic Properties of Sn-Doped TiO2 from First-Principles Calculations. *J. Phys. Chem. C* **2009**, *113* (2), 650−653.

(25) Štengl, V.; Bakardjieva, S. Molybdenum-Doped Anatase and Its Extraordinary Photocatalytic Activity in the Degradation of Orange II in the UV and Vis Regions. *J. Phys. Chem. C* **2010**, *114* (45), 19308−19317.

(26) Khan, M.; Xu, J.; Chen, N.; Cao, W. First Principle Calculations of the Electronic and Optical Properties of Pure and (Mo, N) Co-Doped Anatase TiO2. *J. Alloys Compd.* **2012**, *513*, 539−545.

(27) Shi, W.; Chen, Q.; Xu, Y.; Wu, D.; Huo, C. F. Investigation of the Silicon Concentration Effect on Si-Doped Anatase TiO2 by First-Principles Calculation. *J. Solid State Chem.* **2011**, *184* (8), 1983−1988.

(28) Blöchl, P. E. Projector Augmented-Wave Method. *Phys. Rev. B* **1994**, *50* (24), 17953−17979.

(29) Kertesz, M.; Kresse, G. Performance of the Vienna ab initio simulation package (VASP) in chemical applications. *J. Mol. Struct.* **2003**, *624*, 37.

(30) Perdew, J. P.; Burke, K.; Ernzerhof, M. Generalized Gradient Approximation Made Simple [Phys. Rev. Lett. 77, 3865 (1996)]. *Phys. Rev. Lett.* **1997**, *78* (7), 1396.

(31) Monkhorst, H. J.; Pack, J. D. Special Points for Brillouin-Zone Integrations. *Phys. Rev. B* **1976**, *13* (12), 5188−5192.

(32) Heyd, J.; Scuseria, G. E.; Ernzerhof, M. Hybrid Functionals Based on a Screened Coulomb Potential. *J. Chem. Phys.* **2003**, *118* (18), 8207−8215.

(33) Momma, K.; Izumi, F. VESTA 3 for Three-Dimensional Visualization of Crystal, Volumetric and Morphology Data. *J. Appl. Crystallogr.* **2011**, *44* (6), 1272−1276.

(34) Arroyo-De Dompablo, M. E.; Morales-García, A.; Taravillo, M. DFT+*U* calculations of crystal lattice, electronic structure, and phase stability under pressure of TiO2 polymorphs. *J. Chem. Phys.* **2011**, *135* (5), 054503.

(35) Horn, M.; Schwerdtfeger, C. F.; Meagher, E. P. Refinement of the Structure of Anatase at Several Temperatures*. *Z. Kristallogr.* **1972**, *136*, 273.

(36) Tosoni, S.; Lamiel-Garcia, O.; Fernandez Hevia, D.; Doña, J. M.; Illas, F. Electronic Structure of F-Doped Bulk Rutile, Anatase, and Brookite Polymorphs of TiO 2. *J. Phys. Chem. C* **2012**, *116* (23), 12738−12746.

(37) Van De Walle, C. G.; Neugebauer, J. First-Principles Calculations for Defects and Impurities: Applications to III-Nitrides. *J. Appl. Phys.* **2004**, *95* (8), 3851−3879.

(38) Wang, Y.; Zhang, R.; Li, J.; Li, L.; Lin, S. First-Principles Study on Transition Metal-Doped Anatase TiO 2. *Nanoscale Res. Lett.* **2014**, *9*, 46.

(39) Nair, R. G.; Das, A.; Paul, S.; Rajbongshi, B.; Samdarshi, S. K. MWCNT Decorated V-Doped Titania: An Efficient Visible Active Photocatalyst. *J. Alloys Compd.* **2017**, *695*, 3511−3516.

(40) Lippens, P. E.; Chadwick, A. V.; Weibel, A.; Bouchet, R.; Knauth, P. Structure and Chemical Bonding in Zr-Doped Anatase TiO2 Nanocrystals. *J. Phys. Chem. C* **2007**, *112* (1), 43−47.

(41) Tio, A.; Guo, M.; Du, J. First-principles study of electronic structures and optical properties of Cu, Ag, and Au-doped anatase TiO2. *Phys. B Condens. Matter* **2012**, *407* (6), 1003−1007.

(42) Chen, H.; Li, X.; Wan, R.; Kao-Walter, S.; Lei, Y. A DFT Study of the Electronic Structures and Optical Properties of (Cr, C) Co-Doped Rutile TiO2. *Chem. Phys.* **2018**, *501*, 60−67.

(43) Ma, X.; Xue, L.; Yin, S.; Yang, M.; Yan, Y. Preparation of V-Doped TiO2 Photocatalysts by the Solution Combustion Method and Their Visible Light Photocatalysis Activities. *J. Wuhan Univ. Technol., Mater. Sci. Ed.* **2014**, *29* (5), 863−868.

(44) Kernazhitsky, L.; Shymanovska, V.; Gavrilko, T.; Naumov, V.; Fedorenko, L.; Kshnyakin, V.; Baran, J. Photoluminescence of Cr-Doped TiO2 Induced by Intense UV Laser Excitation. *J. Lumin.* **2015**, *166* (October), 253−258.

(45) Okoye, C. M. I. First-Principles Optical Calculations of AsNMg3 and SbNMg3. *Mater. Sci. Eng., B* **2006**, *130* (1−3), 101−107.

(46) Saha, S.; Sinha, T. P.; Mookerjee, A. Electronic Structure, Chemical Bonding, and Optical Properties of Paraelectric ${\mathrm{BaTiO}}_{3}$. *Phys. Rev. B* **2000**, *62* (13), 8828−8834.

(47) Yu, X.; Li, C.; Ling, Y.; Tang, T. A.; Wu, Q.; Kong, J. First Principles Calculations of Electronic and Optical Properties of Mo-Doped Rutile TiO2. *J. Alloys Compd.* **2010**, *507* (1), 33−37.

(48) Klosek, S.; Raftery, D. Visible Light Driven V-Doped TiO2 Photocatalyst and Its Photooxidation of Ethanol. *J. Phys. Chem. B* **2001**, *105* (14), 2815−2819.

(49) Su, Y.; Chen, S.; Quan, X.; Zhao, H.; Zhang, Y. A Silicon-Doped TiO2 Nanotube Arrays Electrode with Enhanced Photo-electrocatalytic Activity. *Appl. Surf. Sci.* **2008**, *255* (5), 2167−2172.

(50) Van Viet, P.; Huy, T. H.; You, S. J.; Van Hieu, L.; Thi, C. M. Hydrothermal Synthesis, Characterization, and Photocatalytic Activity of Silicon Doped TiO2 Nanotubes. *Superlattices Microstruct.* **2018**, *123*, 447−455.

(51) Kim, D. S.; Yang, J. H.; Balaji, S.; Cho, H. J.; Kim, M. K.; Kang, D. U.; Djaoued, Y.; Kwon, Y. U. Hydrothermal Synthesis of Anatase Nanocrystals with Lattice and Surface Doping Tungsten Species. *CrystEngComm* **2009**, *11* (8), 1621−1629.

(52) Stengl, V.; Velická, J.; Maříková, M.; Grygar, T. M. New Generation Photocatalysts: How Tungsten Influences the Nanostructure and Photocatalytic Activity of TiO2 in the UV and Visible Regions. *ACS Appl. Mater. Interfaces* **2011**, *3* (10), 4014−4023.

(53) Peng, H.; Li, J.; Li, S. S.; Xia, J. B. First-Principles Study of the Electronic Structures and Magnetic Properties of 3d Transition Metal-Doped Anatase TiO2. *J. Phys.: Condens. Matter* **2008**, *20* (12), 125207.

(54) Hong, N. H.; Sakai, J.; Hassini, A. Ferromagnetism at Room Temperature with a Large Magnetic Moment in Anatase V-Doped TiO2 Thin Films. *Appl. Phys. Lett.* **2004**, *84* (14), 2602−2604.

(55) Ravi, S.; Winfred Shashikanth, F. Magnetic Properties of Mo-Doped TiO2 Nanoparticles: A Candidate for Dilute Magnetic Semiconductors. *Mater. Lett.* **2020**, *264*, 127331.